Supplementary Information

Robust Doping of Single-Walled Carbon Nanotubes with Ionic Liquids: Experiment and First-Principles Modeling

Bogumiła Kumanek[a,§,*], Karolina Z. Milowska[b,c,d,§,*], Marta Stachura[a], Tomasz Wasiak[a], Karolina Matuszek[e], Mike C. Payne[b], Douglas MacFarlane[e], Dawid Janas[a,*]

[a] Department of Organic Chemistry, Bioorganic Chemistry and Biotechnology, Silesian University of Technology, B. Krzywoustego 4, 44-100 Gliwice, Poland

[b] TCM Group, Cavendish Laboratory, University of Cambridge, 19 JJ Thomson Avenue, Cambridge CB3 0HE, United Kingdom

[c] CIC nanoGUNE, Donostia-San Sebastián 20018, Spain

[d] Ikerbasque, Basque Foundation for Science, Bilbao 48013, Spain

[e] Monash University, School of Chemistry, Clayton, VIC 3800, Australia

§ both authors contributed equally

* Corresponding authors: bogumila.kumanek@polsl.pl; kz.milowska@nanogune.eu, dawid.janas@polsl.pl

1. Manufacture of SWCNT films and characterization by Raman spectroscopy/SEM

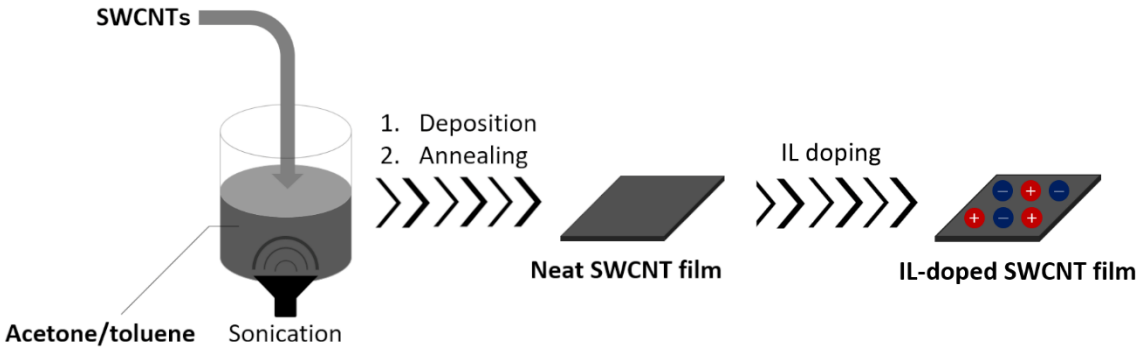

Figure S1 Synthesis and IL-doping of SWCNT films.

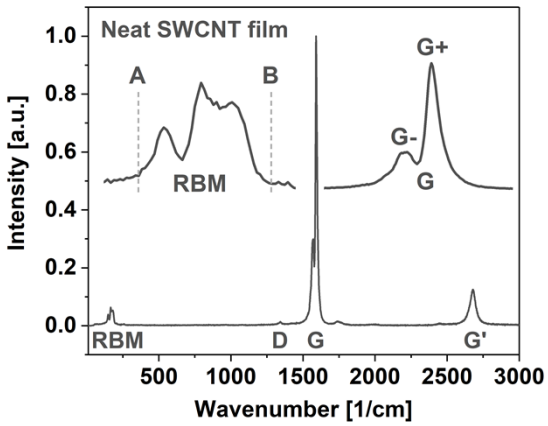

Figure S2 Raman spectrum of a neat SWCNT film. The insets show magnified RBM and G peak areas.

Table S1. I_D/I_G ratios of the IL-doped SWCNT films as compared with the pristine material.

Sample code	IL dopant	I_D/I_G [-]
Neat SWCNT film	-	0.01
A1	tetramethylammonium chloride	0.02
A2	tetramethylammonium iodide	0.01
A3	tetramethylammonium tetrafluoroborate	0.02
A4	tetramethylammonium trifluoromethansulfonate	0.02
A5	tetramethylammonium p-toluenosulfonate	0.01
B6	tetraethylammonium chloride	0.01
B7	tetraethylammonium iodide	0.01
B8	tetraethylammonium tetrafluoroborate	0.02
B9	tetraethylammonium trifluoromethasulfonate	0.01
B10	tetraethylammonium p-toluenosulfonate	0.02
C11	tetrabutylammonium chloride	0.01
C12	tetrabutylammonium iodide	0.01
C13	tetrabutylammonium tetrafluoroborate	0.01
C14	tetrabutylammonium trifluoromethanesulfonate	0.02
C15	tetrabutylammonium p-toluenesulfonate	0.02

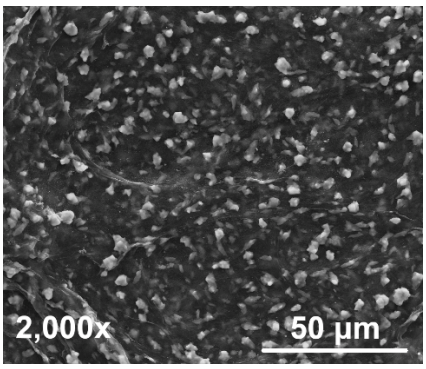

Figure S3 High-resolution SEM micrograph SWCNT film doped with tetramethylammonium iodide (A2).

2. Modeling details

The calculations of structural and electronic properties of pristine and doped SWCNTs have been carried out in the framework of the spin-polarized density functional theory (DFT)[1,2] in the generalized gradient approximation (GGA) approach using Perdew-Burke-Ernzerhof (PBE) parameterization[3] as implemented in QuantumATK [4,5] and Siesta[6,7] numerical packages. Valence electrons were represented with double-ζ numerical basis (DZP) sets of orbitals localized on atoms, with polarization functions also included. The influence of the core electrons was accounted for using norm-conserving Troullier–Martins[8] nonlocal pseudopotentials cast in the Kleinman–Bylander[9] separable form. Long-range interactions between the halogens and the SWCNTs were included in the total bonding energy using the methodology proposed by Grimme [10]. [x] The Brillouin zone was sampled in a 3x3x7 Monkhorst and Pack scheme[11], while the density mesh cut-off for real-space integrals was set to 300 Ry. For the band structure and density of states calculations, the kinetic cut-off for real-space integrals was increased to 500 Ry. During all calculations, the self-consistent field (SCF) cycle was iterated until the density matrix by less than 10^{-5} per iteration. Models presented in Fig. ST1 were optimized until a maximum force converged to lower than 0.004 eV/Å and the total energy changed by less than 10^{-5} eV. The simulations were performed using 3D periodic boundary conditions.

The thermoelectric properties of the most stable systems were calculated employing DFT in combination with the non-equilibrium Green's function method (NEGF) as implemented in QuantumATK[4,12–14]. The basis sets were reduced to single- ζ with polarization functions (SZP), while other parameters remain the same as during structural and electronic properties calculations. Pure and doped SWCNTs comprising the central scattering regions of device configurations were coupled to two semi-infinite silver electrodes, as shown in Fig. ST3, top panels. The interfaces between the Ag (001) surfaces and the SWCNT open ends were fully relaxed until a maximum force converged to lower than 0.01 eV/Å and the maximum stress changed by less than 0.1 GPa.

The Brillouin zone of the two-probe system was sampled using a 1 × 1 × 100 Monkhorst–Pack scheme. The transmission spectra were calculated in the [−3,3] eV range within 601 points.

The thermoelectric properties were calculated using linear response theory[15,16]. In this approximation, the Landauer–Büttiker formula for electrical current in the ballistic regime is expressed as the sum of two terms:

$$I = \Delta\mu\frac{2e}{h}\int_{-\infty}^{\infty}\overline{T}(\varepsilon,U)\frac{\partial f(\varepsilon,U,T)}{\partial\mu}d\varepsilon + \Delta T\frac{2e}{h}\int_{-\infty}^{\infty}\overline{T}(\varepsilon,U)\frac{\partial f(\varepsilon,U,T)}{\partial T}d\varepsilon,$$

where U is a finite bias voltage, e is the electron charge, h is the Planck constant, $\overline{T}(\varepsilon,U)$ is the energy-resolved transmission function, f(ε,μ,T) is the Fermi-Dirac electron distribution, μ is the electrochemical potential of the electrode, and T is the temperature of the electrode. ΔT and Δμ are small changes. Chemical potential is expressed as: $\mu = \varepsilon_F \pm eU/2$, where ε_F is the Fermi energy. The transmission function for electrons with energy ε incident in the central region of the device can be expressed by retarded Green's function $\check{G}(\varepsilon)$:

$$\overline{T}(\varepsilon,U) = Tr\left[\check{G}(\varepsilon)\check{\Gamma}_L(\varepsilon,U)\check{G}(\varepsilon)^{\dagger}\check{\Gamma}_R(\varepsilon,U)\right],$$

where $\check{\Gamma}_{L(R)}(\varepsilon,U) = i\left(\check{\Sigma}_{L(R)}(\varepsilon,U) - \check{\Sigma}_{L(R)}(\varepsilon,U)^{\dagger}\right)/2,$ is the broadening function for the left (right) electrode, and $\check{\Sigma}_{L(R)}(\varepsilon,U)$ are the corresponding self-energies calculated in the iterative self-consistent approach.

Hence, the electrical conductance, G, and the Seebeck coefficient, S can be calculated as:

$$G = \frac{dI}{dU}\bigg|_{dT=0} = \frac{1}{U}\times\Delta\mu\frac{2e}{h}\int_{-\infty}^{\infty}\overline{T}(\varepsilon,U)\frac{\partial f(\varepsilon,\mu,T)}{\partial\mu}d\varepsilon$$

,

and

$$S = \frac{-dU}{dT}\bigg|_{I=0} = \frac{-1}{e}\times\frac{\frac{2e}{h}\int_{-\infty}^{\infty}\overline{T}(\varepsilon,U)\frac{\partial f(\varepsilon,\mu,T)}{\partial T}d\varepsilon}{\frac{2e}{h}\int_{-\infty}^{\infty}\overline{T}(\varepsilon,U)\frac{\partial f(\varepsilon,\mu,T)}{\partial\mu}d\varepsilon}$$

, respectively. The power factor per SWCNT is defined as GS^2 [17,18].

Thermoelectric properties of SWCNT films were calculated using a simple model of mixed SWCNT circuits adopted from Hayashi and colleagues[18]. The conductance and the Seebeck coefficient in the parallel model containing 90% metallic SWCNTs are defined as:

$$G_{film} = 0.9G_m + 0.1G_S$$

and

$$S_{film} = \frac{0.9G_mS_m + 0.1G_SS_S}{0.9G_m + 0.1G_S},$$

where $G_{m(S)}$ and $S_{m(S)}$ are the conductance and Seebeck coefficients of metallic and semiconducting SWCNTs, as shown in **Fig. T3 (b)**.

Table S2 DFT computed structural and energetic properties of fully optimized pristine and all IL-doped (12,12) and (20,0) SWCNTs shown in **Fig. ST1**. The nitrogen/sulfur-SWCNT distances are the smallest difference between the molecule nitrogen/sulfur distance from the SWCNT symmetry axis and the mean of the SWCNT radius. The coefficient of SWCNT radius variation, CV, is calculated as the ratio of the standard deviation to the mean of the SWCNT radius[19]. The adsorption energy per carbon atom, $E_{ads/NC}$, is defined as the difference between the total energies of fully optimized systems containing functionalized SWCNT and IL molecule and the total energies of isolated SWCNT and IL molecule divided by the number of nanotube carbon atoms. The binding energy per atom, $E_{bind/N}$, is calculated as the difference between the total energies of fully optimized systems (pure or functionalized SWCNTs or IL molecules) and the sum of total atomic energies of the free atom of each type that are present in the systems, divided by the number of all atoms in the system. The most stable doped systems (of lower $E_{ads/NC}$) are highlighted in green color.

SWCNT	IL	IL orientation (A=perpendicular; B=parallel)	N_{IL}-SWCNT distance [Å]	S_{IL}-SWCNT distance [Å]	CV	$E_{ads/NC}$ [eV]	$E_{bind/N}$ [eV]
(12,12)	----		----	----	0.0013	----	-8.300
	A5	A	3.361	3.908	0.0045	-0.0081	-8.080
		B	3.955	3.337	0.0041	-0.0070	-8.079
	B9	A	3.896	3.808	0.0021	-0.0081	-8.051
		B	5.073	4.922	0.0022	-0.0041	-8.049
	B10	A	3.938	3.610	0.0064	-0.0070	-8.006
		B	3.814	3.171	0.0050	-0.0106	-8.008
(20,0)	----		----	----	0.0002	----	-8.297
	A5	A	4.494	3.370	0.0028	-0.0040	-8.054
		B	3.941	3.270	0.0018	-0.0059	-8.055
	B9	A	3.841	3.376	0.0043	-0.0052	-8.024
		B	3.779	3.399	0.0022	-0.0032	-8.023
	B10	A	3.911	3.227	0.0032	-0.0077	-7.977
		B	3.928	3.262	0.0049	-0.0053	-7.976

Table S3 DFT computed electronic properties of fully optimized pristine and chosen IL-doped (12,12) and (20,0) SWCNTs: Fermi levels (E_F), the valence band maxima (VBM) and conduction band minima (CBM) with respect to the Fermi levels of fully optimized pristine (12,12) and (20,0) SWCNTs, energy band gaps (E_{gap}), Hirshfeld charges of SWCNTs (q_H^{SWCNT}), and oxygen impurity levels closest to the Fermi level of each system (E_O). Charge transfer from IL molecule to SWCNT was calculated using Hirshfeld charge population analysis[20,21] on the fully optimized structures. The positive values indicate a deficiency of electrons in SWCNTs after IL doping. The most stable doped systems are highlighted in green color.

SWCNT	IL	IL orientation (A=perpendicular; B=parallel)	E_F [eV]	VBM-E_F^{pure} [eV]	E_F^{pure} -CBM [eV]	E_{gap} [eV]	q_H^{SWCNT} [|e|]	E_O [eV]
(12,12)	----	----	-3.941	0.000	0.000	0.000	---	----
	A5	A	-3.913	0.028	-0.028	0.000	0.084	-0.660
		B	-3.918	0.024	-0.024	0.000	0.107	-0.645
	B9	A	-3.948	-0.007	0.007	0.000	0.092	-0.684
	B10	B	-3.962	-0.021	0.021	0.000	0.147	-0.620
(20,0)	----	----	-3.925	-0.233	-0.238	0.471	---	----
	A5	B	-3.900	-0.205	-0.260	0.465	0.114	-0.760
	B9	A	-3.908	-0.214	-0.252	0.466	0.087	-0.907

	B10	A	-3.904	-0.208	-0.255	0.462	0.138	-0.552

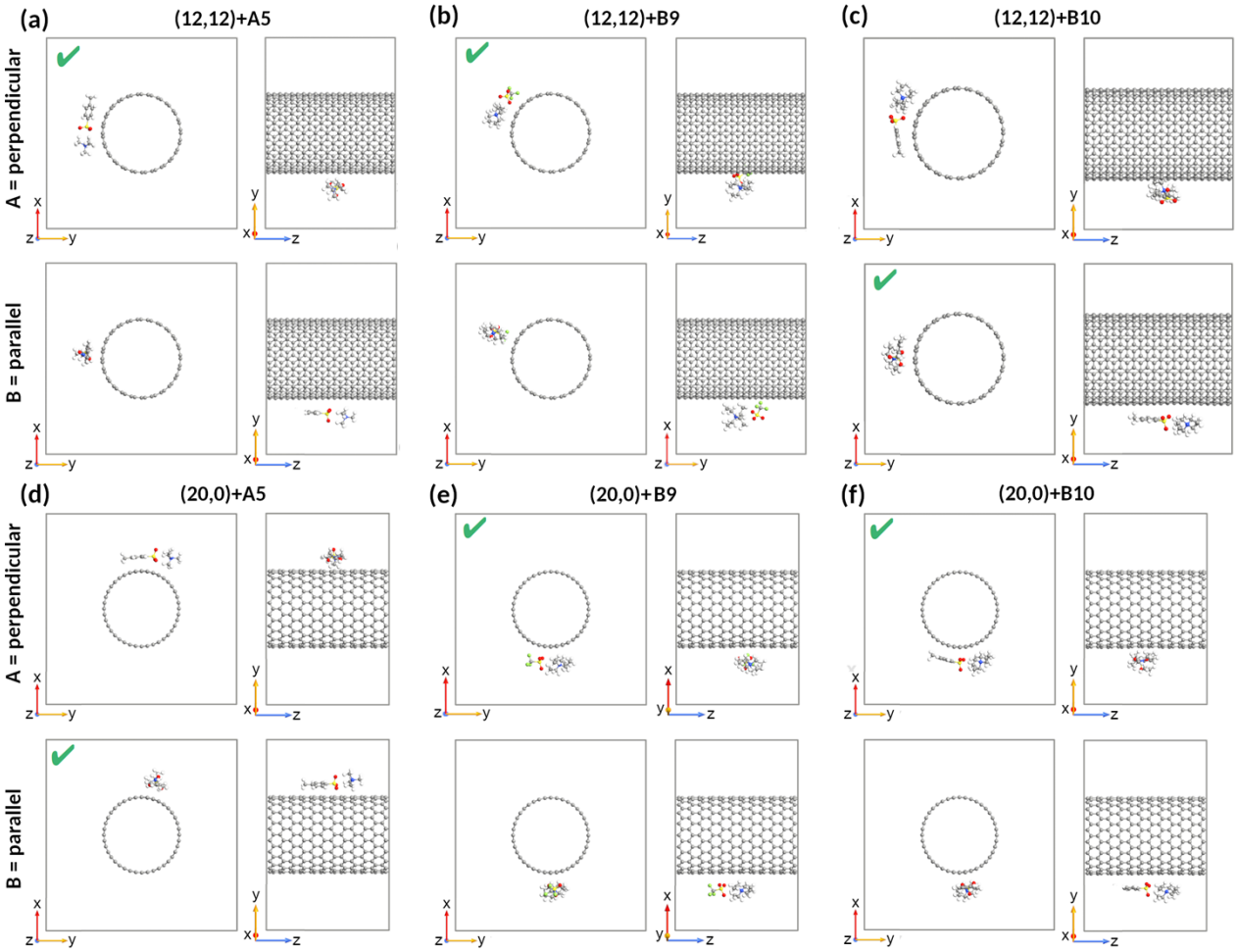

Figure S4 Atomistic cross-sectional and side views of fully optimized (a-c) (12,12) and (d-f) (20,0) SWCNTs interacting with (a,d) A5, B9 (b,e) and (c,f) B10. Supercells are marked by grey lines. C atoms are depicted in grey, while H, N, O, S, and F atoms are shown in white, blue, red, yellow, and green, respectively. The energetically preferable orientations of IL molecules are marked by a green tick.

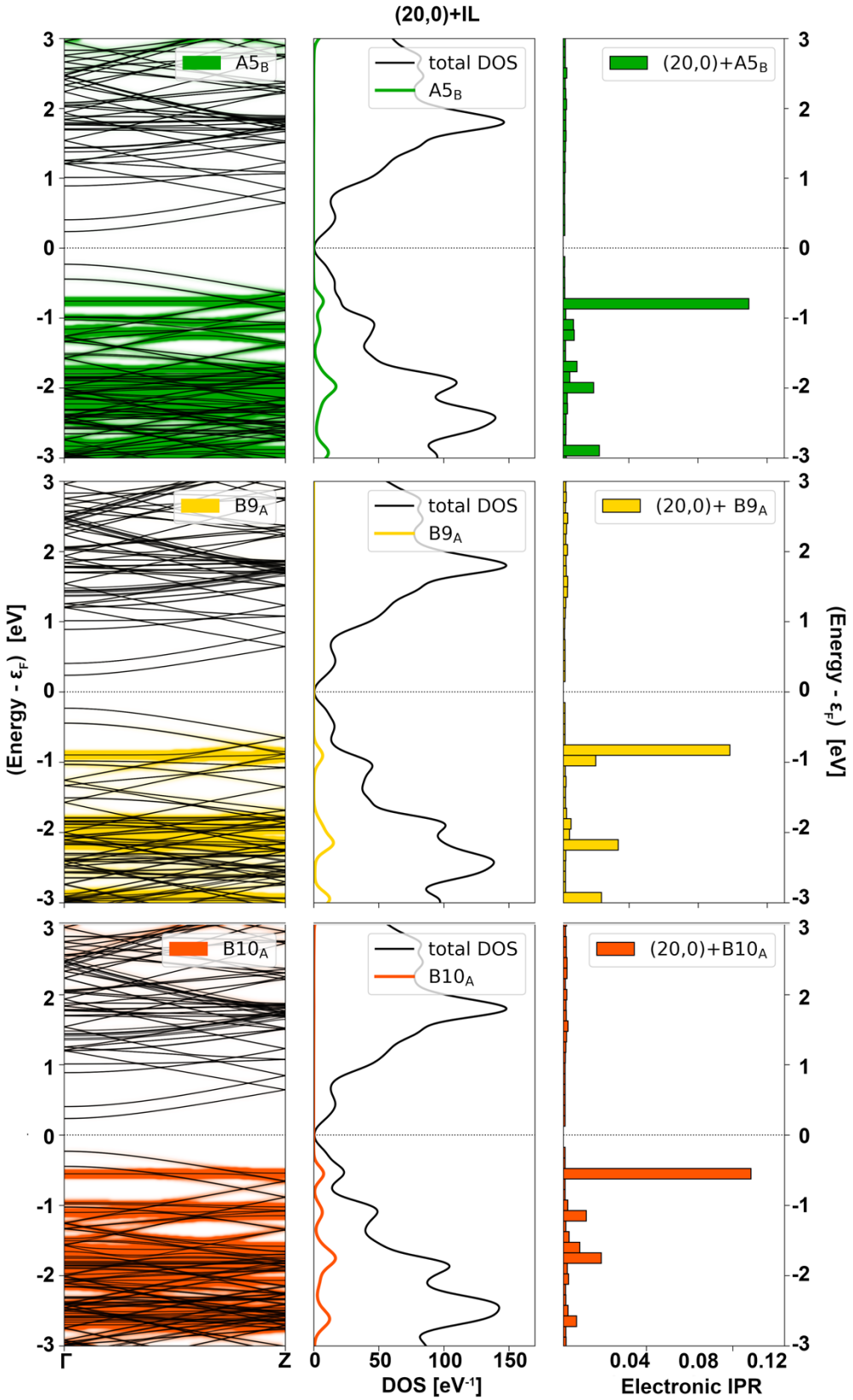

Figure S5 Computed electronic properties of (20,0) SWCNTs doped with A5, B9 and B10 molecules. The fat band structures along Γ → Z of the Brillouin zone, together with the projected density of states on IL molecules (PDOS) and electronic inverse participation ratios (IPR), are plotted for the most stable systems. Only IPR values above 1/N, which correspond to the expected values for delocalized states, are shown. N is the total number of atoms in each supercell. The thickness of IPR bars is set to 0.15 eV. The Fermi level (ε_F) of each system has been shifted to 0.

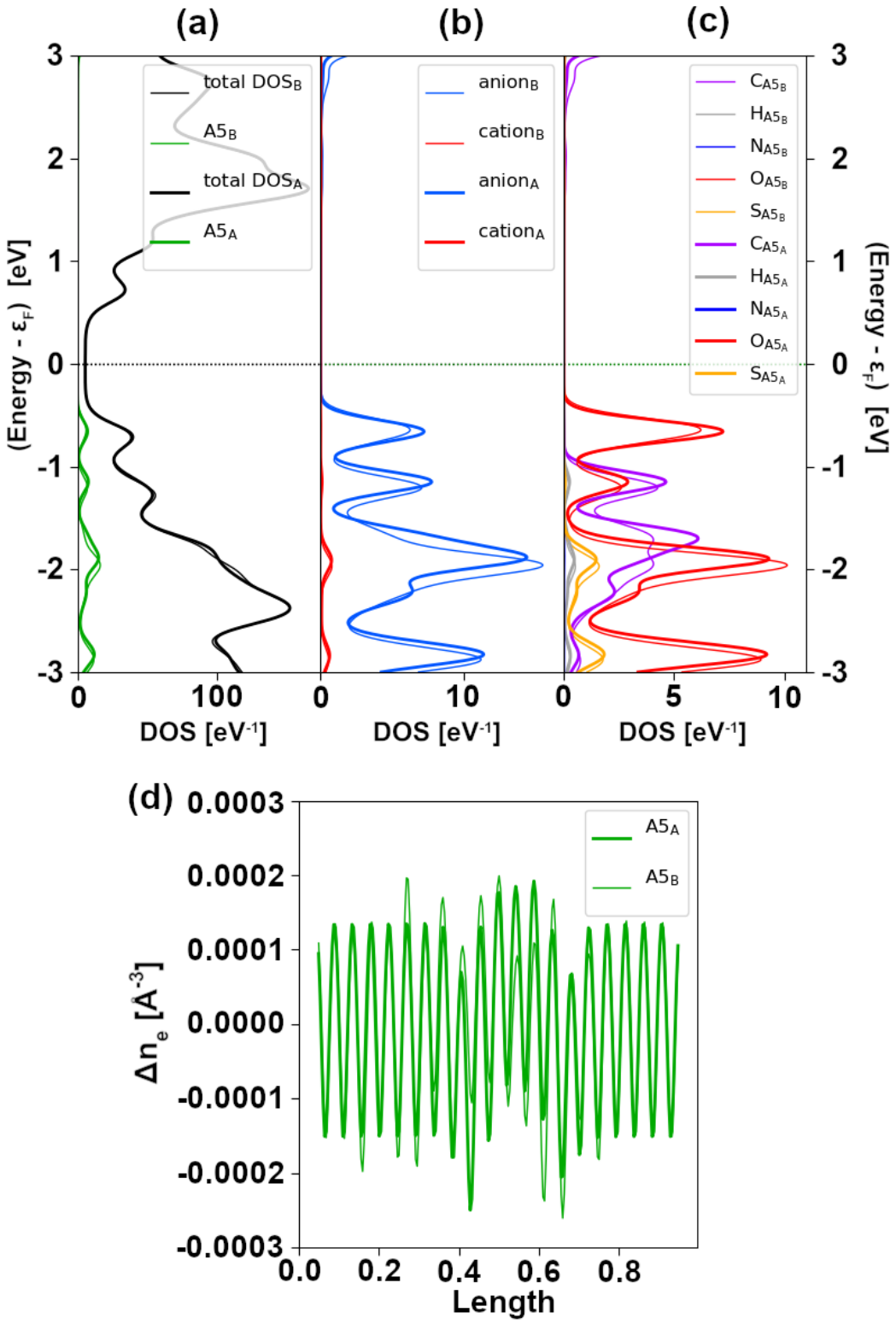

Figure S6 Comparison between DFT computed electronic properties of (12,12) SWCNT doped with A5 molecule in perpendicular (A) and parallel (B) orientations. (a) The total and projected density of states (DOS) on A5 molecules. (b) The projected density of states on anion and cation. (c) The projected density of states on molecule C, molecule H, molecule N, molecule O, and molecule S. (d) The macroscopic averages of 1D projections of electron difference densities (Δn_e) on the z-axis (along SWCNT symmetry axis) for both orientations. The macroscopic average was taken in the range of [0.1, 0.9] of the primitive lattice vector along the z-direction. The DOS and Δn_e of energetically preferable perpendicular configuration are plotted using a thick line.

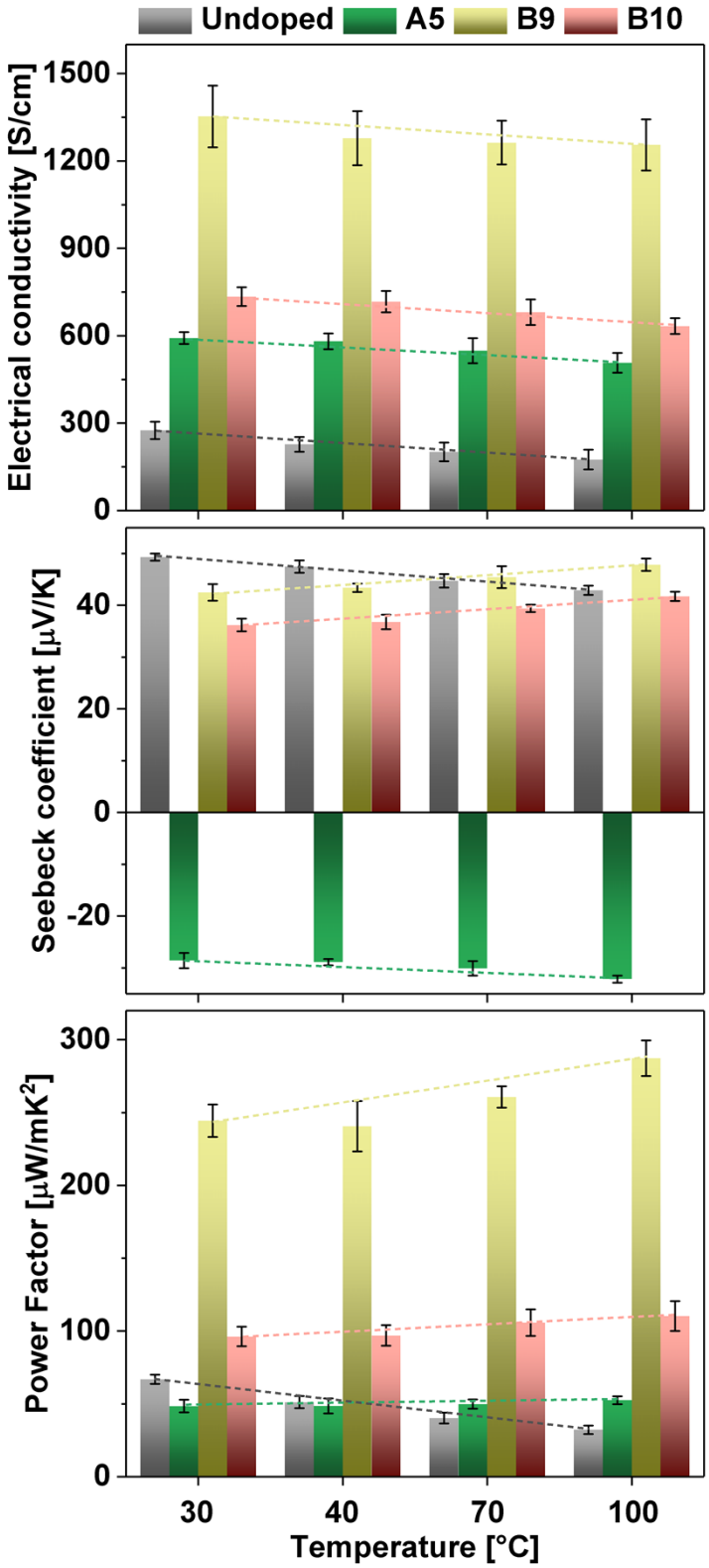

Figure S7 (a) Electrical conductivity, (b) Seebeck coefficient, and (c) PF at different temperatures for a pristine SWCNT film and SWCNT films after doping with A5, B9, and B10 molecules. Lines were added to guide the eye through a selected group of results. The electrical conductivity of all presented samples decreases with increasing temperature and is the highest for B9-doped samples. Seebeck coefficient of B9 and B10 samples increases with increasing temperature and decreases in the case of undoped and A5-doped SWCNT films. Note that the Seebeck coefficient is negative only for A5-doped samples. PF of all doped samples (A5, B9, and B10) increases with increasing temperature, while for undoped SWCNT films, the trend is the opposite. The highest power factor is observed for B9-doped SWCNT films.

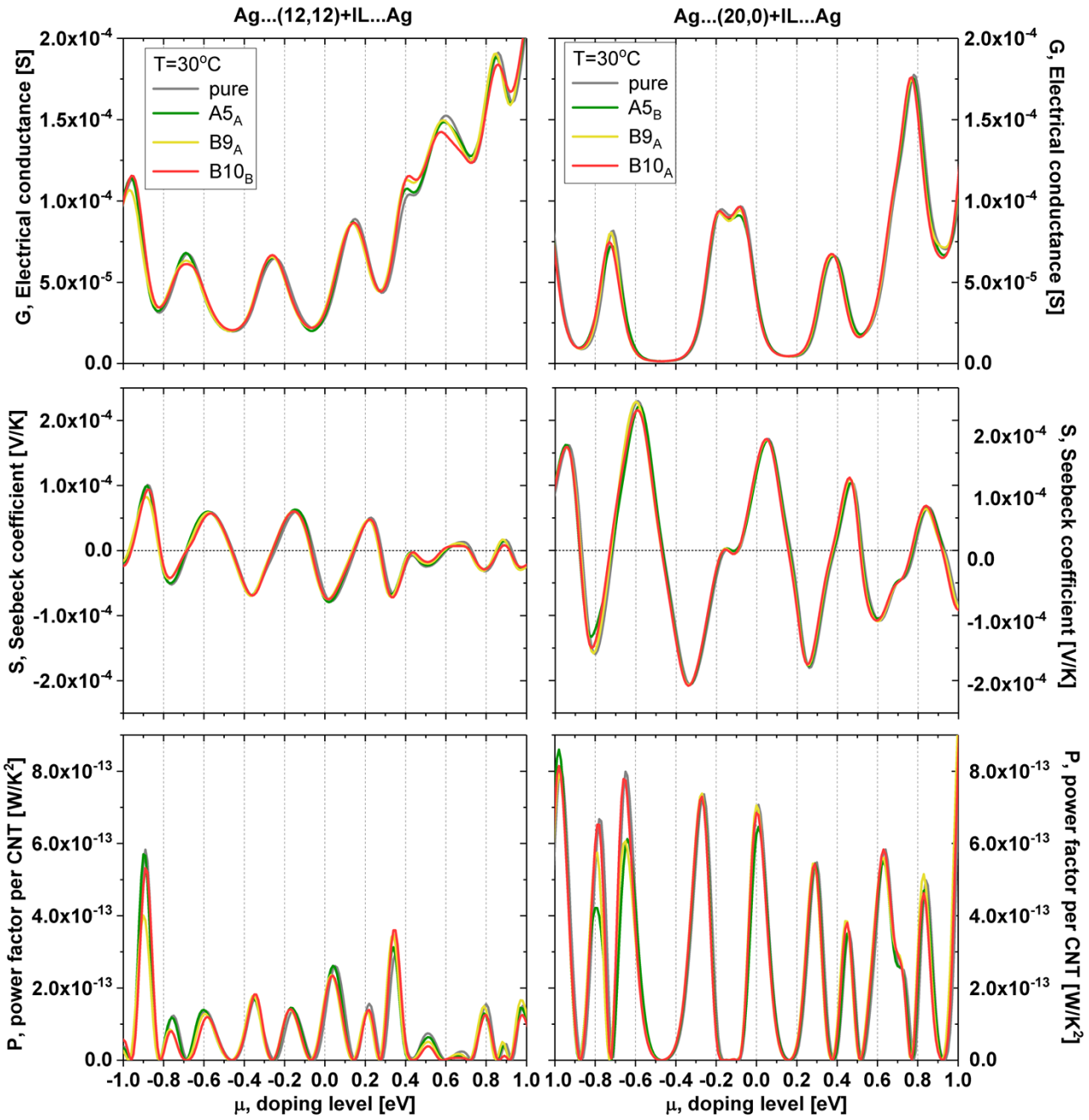

Figure S8 Computed thermoelectric properties of IL doped metallic (12,12) and semiconducting (20,0) SWCNTs coupled to Ag electrodes. Conductance (G), Seebeck coefficient (S), and PF per SWCNT (P) are plotted as a function of doping level (μ) for 30°C. Thermoelectric properties of pristine SWCNTs (grey lines) are shown as a reference.

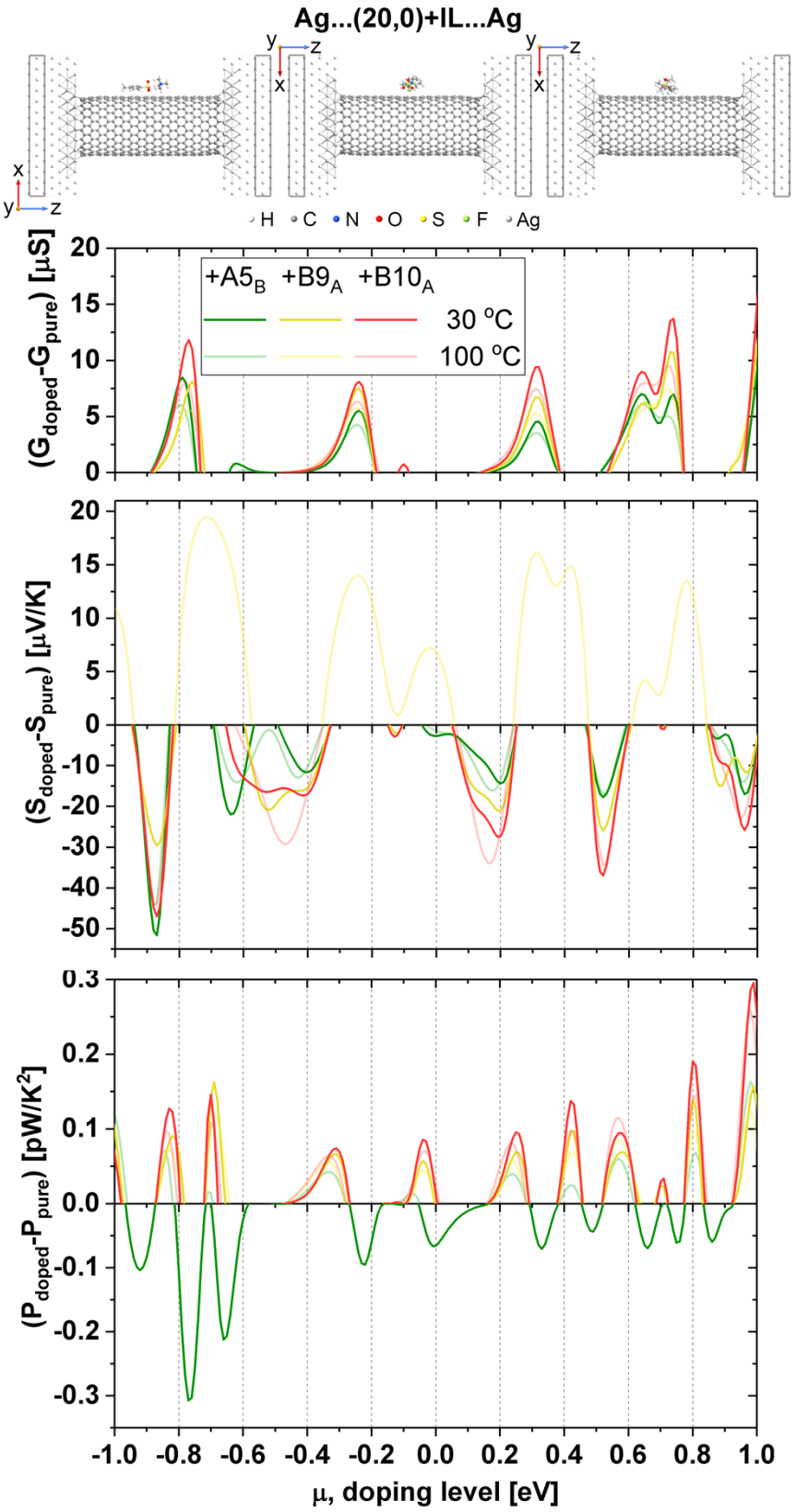

Figure S9 Computed thermoelectric properties of IL-doped semiconducting (20,0) SWCNT sandwiched between Ag (001) layers. The relative changes in conductance, Seebeck coefficient, and PF per nanotube of (20,0) SWCNT functionalized with A5, B9, or B10 are plotted as a function of doping level (μ) for two different temperatures: 30 and 100°C. The changes in G, S, and P are calculated with respect to the pristine device model of (20,0) SWCNT. Atomistic side views of the models used for transport calculations are presented at the top of the figure. The semi-infinite Ag electrodes are outlined in grey.

3. Determination of doping stability

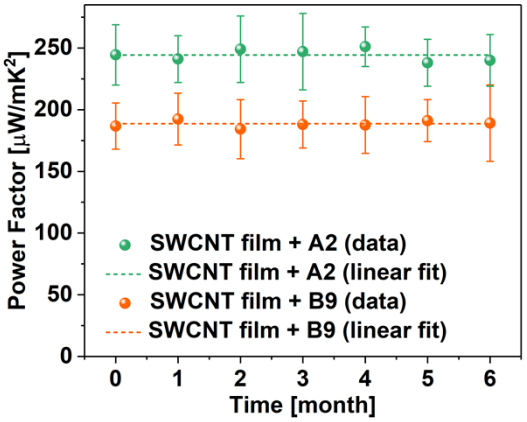

Figure S10 PF values of SWCNT films doped with trifluoromethasulfonate (A2) and tetraethylammonium trifluoromethasulfonate (B9) measured over the course of 6 months.

References

[1] P. Hohenberg, W. Kohn, Inhomogeneous Electron Gas, Phys. Rev. 136 (1964) B864–B871. https://doi.org/10.1103/PhysRev.136.B864.

[2] W. Kohn, L.J. Sham, Self-Consistent Equations Including Exchange and Correlation Effects, Phys. Rev. 140 (1965) A1133–A1138. https://doi.org/10.1103/PhysRev.140.A1133.

[3] J.P. Perdew, K. Burke, M. Ernzerhof, Generalized Gradient Approximation Made Simple, Phys. Rev. Lett. 77 (1996) 3865–3868. https://doi.org/10.1103/PhysRevLett.77.3865.

[4] Synopsis QuantumATK version 2022.03-SP1, https://www.synopsys.com/silicon/quantumatk.html (accessed 10-09-2022), (n.d.).

[5] S. Smidstrup, D. Stradi, J. Wellendorff, P.A. Khomyakov, U.G. Vej-Hansen, M.-E. Lee, T. Ghosh, E. Jónsson, H. Jónsson, K. Stokbro, First-principles Green's-function method for surface calculations: A pseudopotential localized basis set approach, Phys. Rev. B 96 (2017) 195309. https://doi.org/10.1103/PhysRevB.96.195309.

[6] P. Ordejón, E. Artacho, J.M. Soler, Self-consistent order-N density-functional calculations for very large systems, Phys. Rev. B 53 (1996) R10441–R10444. https://doi.org/10.1103/PhysRevB.53.R10441.

[7] J.M. Soler, E. Artacho, J.D. Gale, A. García, J. Junquera, P. Ordejón, D. Sánchez-Portal, The SIESTA method forab initioorder-Nmaterials simulation, Journal of Physics: Condensed Matter 14 (2002) 2745–2779. https://doi.org/10.1088/0953-8984/14/11/302.

[8] N. Troullier, J.L. Martins, Efficient pseudopotentials for plane-wave calculations, Phys. Rev. B 43 (1991) 1993–2006. https://doi.org/10.1103/PhysRevB.43.1993.

[9] L. Kleinman, D.M. Bylander, Efficacious Form for Model Pseudopotentials, Phys. Rev. Lett. 48 (1982) 1425–1428. https://doi.org/10.1103/PhysRevLett.48.1425.

[10] S. Grimme, Semiempirical GGA-type density functional constructed with a long-range dispersion correction, Journal of Computational Chemistry 27 (2006) 1787–1799. https://doi.org/10.1002/jcc.20495.

[11] H.J. Monkhorst, J.D. Pack, Special points for Brillouin-zone integrations, Phys. Rev. B 13 (1976) 5188–5192. https://doi.org/10.1103/PhysRevB.13.5188.

[12] M. Brandbyge, J.-L. Mozos, P. Ordejón, J. Taylor, K. Stokbro, Density-functional method for nonequilibrium electron transport, Phys. Rev. B 65 (2002) 165401. https://doi.org/10.1103/PhysRevB.65.165401.

[13] S. Smidstrup, T. Markussen, P. Vancraeyveld, J. Wellendorff, J. Schneider, T. Gunst, B. Verstichel, D. Stradi, P.A. Khomyakov, U.G. Vej-Hansen, QuantumATK: an integrated platform of electronic and atomic-scale modelling tools, Journal of Physics: Condensed Matter 32 (2019) 015901.

[14] D. Stradi, U. Martinez, A. Blom, M. Brandbyge, K. Stokbro, General atomistic approach for modeling metal-semiconductor interfaces using density functional theory and nonequilibrium Green's function, Phys. Rev. B 93 (2016) 155302. https://doi.org/10.1103/PhysRevB.93.155302.

[15] K. Stokbro, D.E. Petersen, S. Smidstrup, A. Blom, M. Ipsen, K. Kaasbjerg, Semiempirical model for nanoscale device simulations, Phys. Rev. B 82 (2010) 075420. https://doi.org/10.1103/PhysRevB.82.075420.

[16] J.-W. Jiang, J.-S. Wang, B. Li, A nonequilibrium Green's function study of thermoelectric properties in single-walled carbon nanotubes, Journal of Applied Physics 109 (2011) 014326. https://doi.org/10.1063/1.3531573.

[17] D. Hayashi, Y. Nakai, H. Kyakuno, Y. Miyata, K. Yanagi, Y. Maniwa, Temperature dependence of the Seebeck coefficient for mixed semiconducting and metallic single-wall carbon nanotube bundles, Applied Physics Express 13 (2019) 015001. https://doi.org/10.7567/1882-0786/ab547b.

[18] D. Hayashi, Y. Nakai, H. Kyakuno, N. Hongo, Y. Miyata, K. Yanagi, Y. Maniwa, Thermoelectric properties of single-wall carbon nanotube networks, Jpn. J. Appl. Phys. 58 (2019) 075003. https://doi.org/10.7567/1347-4065/ab2408.

[19]K.Z. Milowska, Influence of Carboxylation on Structural and Mechanical Properties of Carbon Nanotubes: Composite Reinforcement and Toxicity Reduction Perspectives, J. Phys. Chem. C 119 (2015) 26734–26746. https://doi.org/10.1021/acs.jpcc.5b08402.
[20]F.L. Hirshfeld, Bonded-atom fragments for describing molecular charge densities, Theoret. Chim. Acta 44 (1977) 129–138. https://doi.org/10.1007/BF00549096.
[21]C. Fonseca Guerra, J.-W. Handgraaf, E.J. Baerends, F.M. Bickelhaupt, Voronoi deformation density (VDD) charges: Assessment of the Mulliken, Bader, Hirshfeld, Weinhold, and VDD methods for charge analysis, Journal of Computational Chemistry 25 (2004) 189–210. https://doi.org/10.1002/jcc.10351.